Hypersonic Shock Wave/Boundary Layer Interactions by a Third-Order Optimized Symmetric WENO Scheme

Li Chen[1,2], *Guo Qilong*[1,2], *Li Qin*[1,2*], *Zhang Hanxin*[1,2]

1. State Key Laboratory of Aerodynamics, China Aerodynamics Research and Development Center,
Mianyang 621000, P. R. China;
2. Computational Aerodynamics Institute, China Aerodynamics Research and Development Center,
Mianyang 621000, P. R. China

(Received 6 July 2016; revised 14 October 2016; accepted 1 November 2016)

Abstract: A novel third-order optimized symmetric weighted essentially non-oscillatory (WENO-OS3) scheme is used to simulate the hypersonic shock wave/boundary layer interactions. Firstly, the scheme is presented with the achievement of low dissipation in smooth region and robust shock-capturing capabilities in discontinuities. The Maxwell slip boundary conditions are employed to consider the rarefied effect near the surface. Secondly, several validating tests are given to show the good resolution of the WENO-OS3 scheme and the feasibility of the Maxwell slip boundary conditions. Finally, hypersonic flows around the hollow cylinder truncated flare (HCTF) and the 25°/55° sharp double cone are studied. Discussions are made on the characteristics of the hypersonic shock wave/boundary layer interactions with and without the consideration of the slip effect. The results indicate that the scheme has a good capability in predicting heat transfer with a high resolution for describing fluid structures. With the slip boundary conditions, the separation region at the corner is smaller and the prediction is more accurate than that with no-slip boundary conditions.

Key words: hypersonic flows; shock wave/boundary layer interactions; weighted essentially non-oscillatory(WENO) scheme; slip boundary conditions

CLC number: V211.3 **Document code**: A **Article ID**: 1005-1120(2017)05-0524-11

0 Introduction

Hypersonic viscous flow interactions between shock wave and boundary layer have been investigated via numerical and experimental approaches[1]. The interactions could cause the formation of a separation region and lead to an increase of heat transfer on the wall near the reattachment point. These effects are necessary to the control and thermal protection of hypersonic vehicles. Recently, North Atlantic Treaty Organization (NATO) Research Technology Organization (RTO) has fostered a series of studies on hypersonic flow interactions. Two configurations chosen for the studies were the hollow cylinder fare and the sharp double cone.

Numerical simulations on these problems are performed by at least two types of approaches nowadays. One type is the kinetic approach including direct simulation Monte Carlo (DSMC) method and some approaches based on the Boltzmann equations. The other type is the continuum approach, e. g. the traditional computational fluid dynamic (CFD) method using Navier-Stokes (N-S) equations. The DSMC method is appropriate for all flow regimes, while the CPU time cost (especially when the Knudsen number is less than 0.001) is relatively huge. Usually solving the N-S equations is about an order of magnitude faster than the DSMC method[2]. However, the N-S equations are invalid in rarefied flow regimes because they are based on the continuum assump-

---

[*] Corresponding author, E-mail address: qin-li@vip.tom.com.

How to cite this article: Li Chen, Guo Qilong, Li Qin, et al. Hypersonic shock wave/boundary layer interactions by a third-order optimized symmetric WENO scheme[J]. Trans. Nanjing Univ. Aero. Astro., 2017,34(5):524-534.
http://dx.doi.org/10.16356/j.1005-1120.2017.05.524

tion. Therefore, it is attractive to find ways to extend the validity of the N-S solver beyond the continuum regime.

Researchers found that the traditional CFD modeling in near continuum regime or slip regime could be improved by using the slip boundary conditions. The most common-used slip boundary conditions were Maxwell[3] slip velocity and Smoluchowski [4] temperature jump boundary conditions. Gökçen and Maccormack et al.[5,6] proposed more general boundary conditions and extended them to larger Knudsen numbers. To correct the linear variability of shear stress near the wall, a wall function approach for boundary condition was proposed by Lockerby et al[7]. Several second-order slip boundary conditions[8,9] were developed to extend the validity of N-S solver. However, it was reported[10] that the second-order slip boundary conditions did not appear to work better than the first-order ones in hypersonic flow simulations.

For N-S solver, developing numerical schemes for shock-capturing is important in hypersonic computation. Nowadays, the total variation diminishing (TVD) schemes, e. g. the non-oscillatory, non-free-parameter and dissipation (NND) scheme[11], are the most widely used in the design phase of hypersonic vehicles. Due to the increasing requirement of accurate prediction on aerodynamics and aerothermodynamics, the weighted essentially non-oscillatory (WENO) scheme proposed by Liu et al.[12] and extended by Jiang and Shu[13] has gained more attentions in recent years[14]. Moreover, some high-order compact schemes were used in the supersonic/hypersonic flows simulation[15,16]. High-order schemes usually need more nodes compared with NND scheme when constructing the flux vectors. For example, it needs seven nodes in the fifth-order WENO scheme, which brings three shortcomings: Causing overshoot in the vicinity of shock wave, being difficult in simulating the flows around complex geometries, and being hard to extend it to the multi-block computational code due to the high order interface boundary condition. Therefore, a five-node scheme, which has high accurate resolution and the number of nodes is the same as NND scheme, is studied here. It costs little to modify from the existing NND codes, and the new third-order scheme aims at engineering computation. In this paper, a new optimized symmetric third-order weighted essentially non-oscillatory (WENO-OS3) scheme is used to simulate hypersonic shock wave/boundary layer interactions.

1 Numerical Methods

1.1 Governing equations

In the generalized computational coordinates (ξ, η, ζ), the dimensionless time-dependent compressible N-S equations can be expressed in the conservative form as follows

$$\frac{\partial \hat{\boldsymbol{Q}}}{\partial t}+\frac{\partial \hat{\boldsymbol{E}}}{\partial \xi}+\frac{\partial \hat{\boldsymbol{F}}}{\partial \eta}+\frac{\partial \hat{\boldsymbol{G}}}{\partial \zeta}=\frac{\partial \hat{\boldsymbol{E}}_{\mathrm{v}}}{\partial \xi}+\frac{\partial \hat{\boldsymbol{F}}_{\mathrm{v}}}{\partial \eta}+\frac{\partial \hat{\boldsymbol{G}}_{\mathrm{v}}}{\partial \zeta} \quad (1)$$

where $\hat{\boldsymbol{Q}}$ is the vector of conservative variables. $\hat{\boldsymbol{E}},\hat{\boldsymbol{F}},\hat{\boldsymbol{G}}$ are inviscid fluxes; and $\hat{\boldsymbol{E}}_{\mathrm{v}},\hat{\boldsymbol{F}}_{\mathrm{v}},\hat{\boldsymbol{G}}_{\mathrm{v}}$ the viscous fluxes. Their definitions are given in Ref. [17].

1.2 WENO-OS3 scheme

An optimized symmetric third-order scheme optimized for inviscid flux term discretization is introduced. The one-dimensional scalar conservation law is used for investigation

$$u_t+f(u)_x=0 \quad (2)$$

With the domain discretized into uniform intervals of Δx, the semi-discretized conservative scheme can be written as

$$(u_t)_j=-\frac{(\hat{f}_{j+1/2}-\hat{f}_{j-1/2})}{\Delta x} \quad (3)$$

where $\hat{f}_{j+1/2}$ approximates $h_{j+1/2}=h(x_{j+1/2})$ to a high-order with $h(u)$ implicitly defined by

$$f(u(x))=\frac{1}{\Delta x}\int_{x-\Delta x/2}^{x+\Delta x/2} h(\xi)\,\mathrm{d}\xi \quad (4)$$

When applied in computation, $f(u)$ is usually split into two parts

$$f(u)=f^{+}(u)+f^{-}(u) \quad (5)$$

In this paper, the Steger-Warming flux vector splitting is used. Then the numerical fluxes are obtained from the positive and negative parts of $f(u)$, namely

$$\hat{f}_{j+1/2}=\hat{f}^{+}_{j+1/2}+\hat{f}^{-}_{j+1/2} \quad (6)$$

where $\hat{f}^{+}_{j+1/2}$ and $\hat{f}^{-}_{j+1/2}$ are computed by WENO-OS3 scheme. We only describe the positive part of the numerical fluxes ($\hat{f}^{+}_{j+1/2}$) here. For simplicity, the superscript "+" is omitted. The negative part of $\hat{f}_{j+1/2}$ is symmetric with respect to $x_{j+1/2}$.

1.2.1 Linear part

In the optimized scheme, an additional candidate stencil is added downwind to that of the third-order WENO (WENO3) scheme. The numerical fluxes are obtained as

$$\hat{f}_{j+1/2}=\alpha_0\hat{f}^{(0)}_{j+1/2}+\alpha_1\hat{f}^{(1)}_{j+1/2}+\alpha_2\hat{f}^{(2)}_{j+1/2} \tag{7}$$

where $\hat{f}^{(i)}_{j+1/2}$ is the approximation of the flux $h_{j+1/2}$ on the ith candidate stencil. The forms of $\hat{f}^{(i)}_{j+1/2}$ are

$$\begin{cases}\hat{f}^{+(0)}_{j+1/2}=f^{+}_{j}+\dfrac{1}{2}\Delta f^{+}_{j-1/2}\\ \hat{f}^{+(1)}_{j+1/2}=f^{+}_{j}+\dfrac{1}{2}\Delta f^{+}_{j+1/2}\\ \hat{f}^{+(2)}_{j+1/2}=f^{+}_{j+1}-\dfrac{1}{2}\Delta f^{+}_{j+3/2}\end{cases} \tag{8}$$

where $\Delta f_{j+1/2}=f_{j+1}-f_{j}$, α_i is the ideal weights of the scheme given by $\alpha_0=\dfrac{1}{3}-\alpha_2,\alpha_1=\dfrac{2}{3}$. After Fourier analysis, we obtain

$$\begin{aligned}\Re[\kappa'(\kappa)]&=\frac{1}{6}(-\sin2\kappa+8\sin\kappa)\\ \Im[\kappa'(\kappa)]&=\frac{1}{2}[-\beta\cos2\kappa+4\beta\cos\kappa-3\beta]\end{aligned} \tag{9}$$

where $\beta=\dfrac{1}{3}-2\alpha_2$, κ is the wavenumber, and κ' the modified wavenumber. $\Re$ and $\Im$ are the real and imaginary part of a complex number, respectively. Because there is one free parameter for a third-order scheme in Eq. (7), the parameter n_{3rd} is introduced to adjust the dissipation level of the scheme. It is suggested that $\Im[\kappa'(\pi)_{\text{WENO-OS3}}]=\dfrac{1}{n_{\mathrm{3rd}}}\Im[\kappa'(\pi)_{\text{WENO3}}]$, then $\alpha_2=\dfrac{(n_{\mathrm{3rd}}-1)}{6n_{\mathrm{3rd}}}$. The scheme turns out to be the WENO3 scheme for $n_{\mathrm{3rd}}=1.0$, and it becomes the fourth-order center difference scheme when $n_{\mathrm{3rd}}\to\infty$. The bigger the n_{3rd} is, the lower the dissipation of WENO-OS3 will be. In this paper, $n_{\mathrm{3rd}}=10$.

1.2.2 Nonlinear part

In order to capture the shock wave and discontinuity, the nonlinear technique should be used. The method used in WENO scheme is employed here, whose idea is to maximize the weight of the smooth candidate stencil while minimize the weight of the discontinuous stencil.

$$\begin{gathered}\hat{f}_{j+1/2}=\sum_{i=0}^{2}\omega_i\hat{f}^{(i)}_{j+1/2}\\ \omega_i=\frac{\Omega_i}{\sum\limits_{k=0}^{2}\Omega_k},\Omega_i=\frac{\alpha_i}{(\varepsilon+IS_i)^{p}}\end{gathered} \tag{10}$$

where IS_i is the smoothness measurement on the ith candidate stencil given by $IS_i=(f_{j+i}-f_{j-1+i})^2$. In the smooth regions, the nonlinear weights are approximately equal to the ideal weights.

Considering the stability of the scheme while decreasing the dissipation error further, the nonlinear weights should be close to the ideal weights as much as possible[13]. To reach this goal, a method with variation of the power in the Eq. (10) was proposed by Li et al[18]. The algorithm is given as follows

$$\begin{gathered}p=\max(p_1,p_2)\\ p_1=TF(|\Delta f^{+}|_{\max};8,p_{11},p_{1\mathrm{u}})\\ p_2=TF(r_{|\Delta f^{+}|_{\max}};8,p_{21},p_{2\mathrm{u}})\\ |\Delta f^{+}|_{\max}=f_{\mathrm{rsc}}(\max_{i=0,\cdots,2}|\sqrt{IS_i}|)\\ r_{|\Delta f^{+}|_{\max}}=\begin{cases}\dfrac{\max_{i=0,\cdots,2}\sqrt{IS_i}}{\varepsilon+\min_{i=0,\cdots,2}\sqrt{IS_i}} & \sqrt{IS_i}\,|_{\max}>r_{\mathrm{u}}p_{11}\\ 1.0 & \text{else}\end{cases}\end{gathered} \tag{11}$$

where p_1 and p_2 are the powers computed by the transition function TF, which is given by

$$TF(x;c,x_1,x_{\mathrm{u}})=1+\tanh\left(\frac{c(x-[(x_{\mathrm{u}}+x_1)/2])}{x_{\mathrm{u}}-x_1}\right) \tag{12}$$

The constant c in Eq. (12) shows the extent of the inclination. x_{u} and x_1 are the upper and lower thresholds, respectively. TF value equals to 2 for $x>x_{\mathrm{u}}$, and it equals to 0 for $x<x_1$. In order to prevent the parameters in the algorithm from being problem-dependent, a specific rescale function f_{rsc} is introduced when p_1 is computed. The function is the same as the corresponding WENO-OS4 scheme given in Ref. [18]. Then, the power is obtained by the maximum of p_1 and p_2. The parameters used in the scheme are calibrated to be: $c=8$, $p_{11}=0.022$, $p_{1\mathrm{u}}=0.029$, $p_{21}=3.2$, $p_{2\mathrm{u}}=3.8$.

A second-order central difference scheme is applied to the viscous fluxes, and the lower-upper symmetric Gauss-Seidel (LU-SGS) method for time approaching is adopted. It is assumed that the gas is perfect gas for all cases in this study, so γ is constant for calculation.

1.3 Slip boundary conditions

Using slip boundary conditions can extend the validity of the N-S solver beyond the continuum regime. The Maxwell boundary condition is first derived for a flat plate[3]. Its generalized form is given by

$$u_s - u_w = \frac{2-\sigma}{\sigma}\lambda\left(\frac{\partial u_\tau}{\partial n} + \frac{\partial u_n}{\partial \tau}\right)_{gw} + \frac{3}{4}\,\frac{\mu}{\rho_{gw} T_{gw}}\left(\frac{\partial T}{\partial \tau}\right)_{gw} \tag{13}$$

where n and τ are the direction normal and tangential to the wall, respectively. u_s is the slip velocity, u_w the wall velocity, σ the momentum accommodation coefficient, and u_τ the tangential velocity along the wall. The subscript "gw" means the physical quantities of gas at the surface. λ refers to the mean free path calculated from local gas flow properties

$$\lambda = \frac{2\mu}{\rho \bar{c}} = \frac{2\mu}{\rho\sqrt{\dfrac{8RT}{\pi}}} \tag{14}$$

where $\bar{c}$ is the mean molecular speed and R the gas constant. For an isothermal wall, it is simplified as

$$u_s - u_w = \frac{2-\sigma}{\sigma}\lambda\left(\frac{\partial u_\tau}{\partial n}\right)_{gw} \tag{15}$$

The temperature jump boundary condition at the wall is given by

$$T_s - T_w = \frac{2-\alpha}{\alpha}\,\frac{2\gamma}{(\gamma+1)Pr}\lambda\left(\frac{\partial T}{\partial n}\right)_{gw} \tag{16}$$

where α is the thermal momentum accommodation coefficient. The following results are calculated by assuming a fully diffuse wall with a corresponding accommodation coefcient of 1.0.

2 Validating Tests

The non-dimensional coefficients related to the results are defined as

$$C_p = \frac{p-p_\infty}{\frac{1}{2}\rho_\infty u_\infty^2},\quad C_h = \frac{q}{\frac{1}{2}\rho_\infty u_\infty^3},\quad St = \frac{q}{\rho_\infty u_\infty (H_0 - H_w)} \tag{17}$$

where the subscript "∞" represents the freestream parameter, and "w" indicates the physical quantities at the wall. C_p is the pressure coefficients, C_h the heat transfer coefficient, St the Stanton number, and H the enthalpy.

2.1 Shu-Osher problem

The test problem for the propagation of the shock wave with Mach number of 3 into smooth density fluctuations was first proposed by Shu and Osher[19]. The test aims at accurately resolving the small scale structures behind the shock. The initial conditions on the domain $-4.5 \leqslant x \leqslant 4.5$ are as follows: $u=0.0$, $p=1.0$, and $\rho = 1 + 0.2\sin(5x)$ for $x \geqslant -4.0$; $u=2.629\,369$, $p=10.333\,33$, and $\rho=3.857\,143$ for $x < -4.0$. The governing equations are one dimensional Euler equations simplified from Eq. (1). A third-order TVD Runge-Kutta method is used for temporal discretization in this case.

Solutions are obtained at $t = 1.8$. Density fields on 800 mesh nodes from NND[11], WENO3 and WENO-OS3 schemes are shown in Fig. 1. The "exact" solution is obtained by the fifth-order WENO scheme on 1 600 mesh nodes. In contrast, NND scheme yields excessively damped solutions, and the WENO3 solutions are less dissipative than that of NND. Similar results are found for WENO-OS3 scheme with better predictions of the wave amplitudes than the original WENO3 scheme.

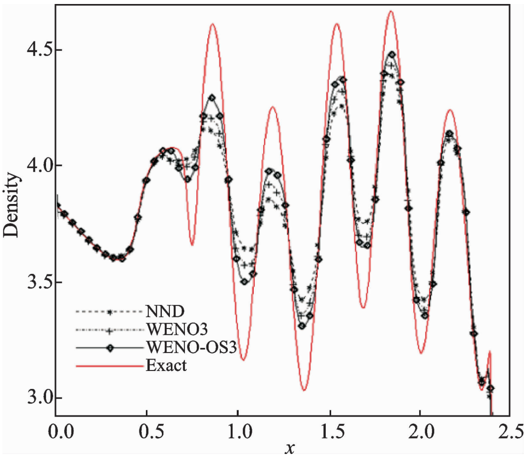

Fig. 1 Density fields at $t = 1.8$ on 800 mesh nodes

2.2 Flat plate shock wave/boundary layer interaction problem

This test problem, an incident shock wave interacting with a boundary layer on a flat plate, has become a benchmark of testing new numerical schemes since it is first proposed in Ref. [20].

The computational parameters are: $Ma_\infty = 2.0$, $Re_\infty = 2.96\times10^5$, $T_\infty = 293.0$ K, $Pr = 0.72$. The impinging shock angle is 32.585°. The computational domain is chosen to be $0 \leqslant x \leqslant 2.02$, $0 \leqslant y \leqslant 1.30$. The number of mesh points used in this paper is 103×122 in the streamwise and the normal directions, respectively. The adiabatic wall boundary condition is adopted.

Fig. 2 presents the pressure contours and patterns of the separation bubble by different numerical schemes. It can be observed that the NND scheme does not capture the separation region with the same mesh, and the size of the bubble decreases with the dissipation of the scheme, i. e. $L_{\text{WENO5}} > L_{\text{WENO-OS3}} > L_{\text{WENO3}} > L_{\text{NND}}$.

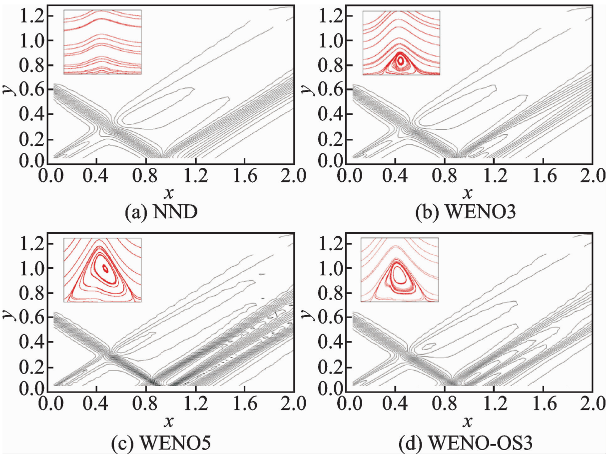

(a) NND (b) WENO3 (c) WENO5 (d) WENO-OS3

Fig. 2 Pressure contours and patterns of the separation bubble by different numerical schemes

2.3 Test for slip boundary conditions

Hypersonic flow of argon over a flat plate at 0° angle of attack which has a previous set of experiments[21] is computed by the WENO-OS3 scheme here. The freestream parameters are $Ma_\infty = 12.7$, $T_\infty = 64.5$ K, $T_w = 292$ K, $p_\infty = 3.73$ Pa, $\lambda_\infty = 0.23$ mm. The Sutherland law is used for modeling the dynamic viscosity in this case, i. e. $\mu = A_s \dfrac{T^{1.5}}{(T+T_s)}$, where $A_s = 1.93\times 10^{-6}$ (Pa • s • $\text{K}^{-1/2}$), and $T_s = 142$ K. The Prandtl number is 0.67, and γ is 1.67. The mesh of 200×140 nodes in x and y directions is used here.

Fig. 3 shows the slip velocity and temperature jump along the surface. By comparison, the results of Maxwell slip boundary conditions agree well with those calculated by Nam et al [10].

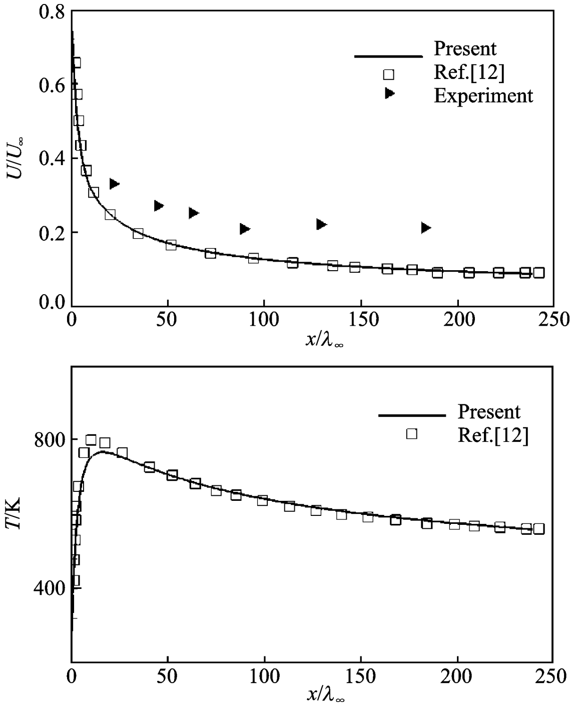

Fig. 3 The gas slip velocity and temperature along the flat plate surface

3 Hypersonic Shock/ Boundary Layer Interactions

A continuum breakdown parameter, the gradient-length local Knudsen number (Kn_{GLL}), defined by Boyd et al. [22] is used for visualizing the rarefied regions in the flow field here

$$Kn_{\text{GLL}} = \frac{\lambda}{Q}\left|\nabla Q\right| \tag{18}$$

where Q is a physical quantity of interest such as pressure, temperature or density. The density is chosen in this paper. It is assumed that continuum breakdown occurs when Kn_{GLL} is greater than 0.05.

3.1 Hollow cylinder truncated flare

Hypersonic flow of nitrogen around a hollow cylinder truncated flare (HCTF) which has a previous set of computational results[23-26] and experiments[23] is calculated here. The configuration and the computational sample mesh structure are shown in Fig. 4. The reference length is $L=101.7$ mm. The freestream parameters are $Ma_\infty=9.91$, $Re_\infty=1.86\times10^5$/m, $T_\infty=51$ K, $T_w=293$ K, which ensure a laminar flow condition. The Sutherland law is used for modeling the dynamic viscosity, where $A_s=1.4\times10^{-6}$ Pa • s • $K^{-1/2}$, and $T_s=106.7$ K. The Prandtl number is 0.71.

The parameters of the inlet flow and top boundaries are set from the freestream. The zero gradient extrapolation method is used to the outflow boundary. At the bottom boundary in front of the leading edge, the symmetric boundary condition is adopted.

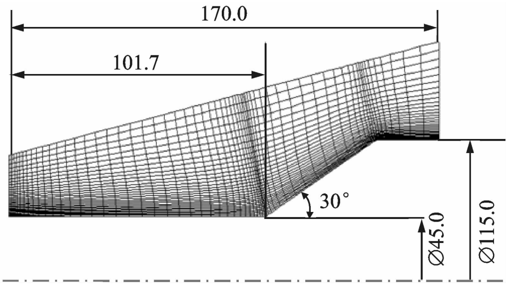

Fig. 4 The configuration and the mesh structure of HCTF (unit: mm)

3.1.1 Flow structures

Typical results of all cases are given in Table 1, where similar flow structures are obtained. The numerical schlieren chart and the streamlines at the corner for the HCTF case are presented in Fig. 5. A strong viscous interaction occurs at the leading edge of HCTF, forming the laminar boundary. A recirculation zone is observed at the corner where it starts near $x/L=0.7$ and ends near $x/L=1.3$. The leading edge shock wave, the separation shock wave and the reattachment shock wave interact with each other near the end of the conical part. The expansion waves are observed at the second corner.

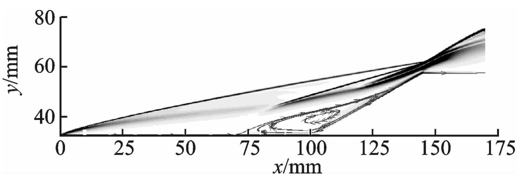

Fig. 5 Numerical schlieren chart and streamlines at the corner

3.1.2 Mesh convergence

To investigate the mesh convergence, three different meshes are conducted, i. e. a coarse mesh (128×128), a medium mesh (256×256), and a fine mesh (512×256). The computations with aforementioned meshes are denoted as CFD1, CFD2 and CFD3, respectively. Table 1 presents the positions of the separation points (X_s) and reattachment points (X_r) using different meshes and different wall boundary conditions. Good mesh convergence can be observed, and the recirculation region length increases with the mesh refinement. The converged results of the N-S equations are a little bigger than DSMC results[23] and experimental results[23]. The disagreement may be the influence of nonequilibrium effects, which is neglected when using Eq. (1), and the inadequacy of slip boundary conditions when simulating the rarefication effects at hypersonic flows. Similar CFD results were also reported in Refs. [23, 24]. Figs. 6, 7 show the pressure coefficient and Stanton number along the surface with the three meshes using no-slip boundary conditions. The results computed by the medium mesh (CFD2) coincide with those by the fine mesh (CFD3), which also indicates that the computation of the mesh converges.

Table 1 Separation and reattachment point locations for different cases of HCTF

Case	Mesh	Wall BCs	X_s/L	X_r/L
CFD1	128×128	No-slip	0.745	1.336
CFD2	256×256	No-slip	0.718	1.345
CFD3	512×256	No-slip	0.718	1.345
CFD1-S	128×128	Slip	0.765	1.329
CFD2-S	256×256	Slip	0.727	1.341
CFD3-S	512×256	Slip	0.726	1.342
DSMC[23]	—	—	0.77	1.32
Experiment [23]	—	—	0.76±0.01	1.34±0.015

3.1.3 Computations with slip boundary conditions

Fig. 8 shows the Kn_{GLL} contours of HCTF which is computed from the density field of CFD3. The gray regions and black regions corresponding to $Kn_{\mathrm{GLL}}>0.05$ are observed in the leading edge, in the shock region and in a thin

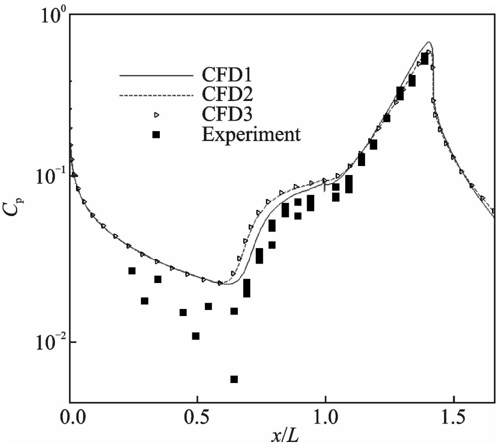

Fig. 6 Pressure coefficient along the surface

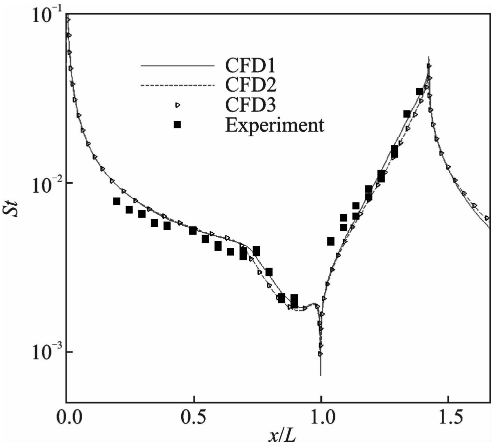

Fig. 7 Stanton number along the surface

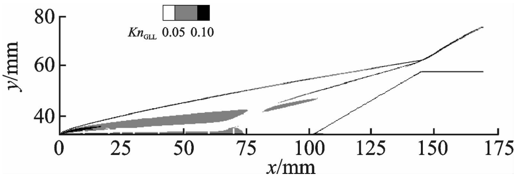

Fig. 8 Kn_{GLL} field for HCTF

boundary layer along the surface. It means the continuum assumption breakdown. Therefore, the slip boundary conditions are adopted for comparison.

Fig. 9 presents the distribution of the slip velocity u_s along the surface by using the Maxwell boundary conditions. The $|U|$ in Fig. 9 refers to velocity magnitude along the wall, the negative parts mean the recirculation region where $u < 0$. The slip velocity appears larger than the gas velocity of the DSMC result. This disagreement is due to the inaccurate physical model within the Knudsen layer. After calculating from a simple relation[24] $u_g = 0.696 u_s$ derived from the linearized Boltzmann equation, the gas velocity is in good agreement with the DSMC result. The wall quantities using different boundary conditions are show in Figs. 10, 11. It can be seen that the results of slip boundary conditions agree better than those of no-slip boundary conditions. With slip boundary conditions, the separation region is smaller than that with no-slip boundary condi-

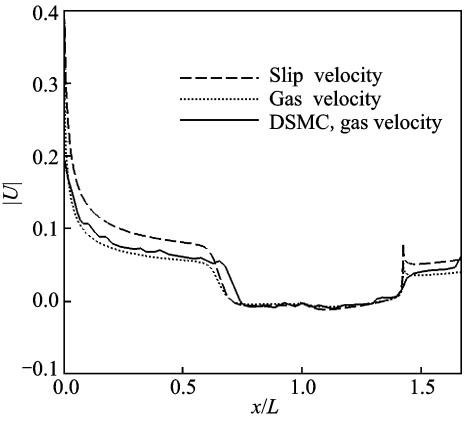

Fig. 9 Slip velocity along the surface for HCTF

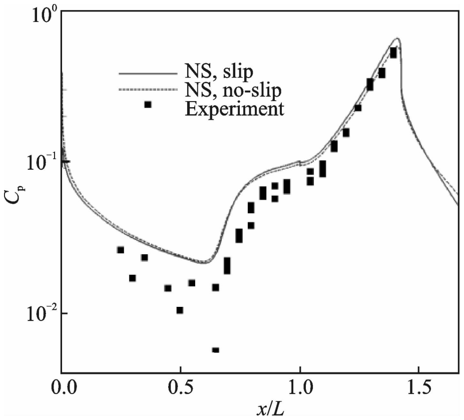

Fig. 10 Pressure coefficient along the surface using different boundary conditions

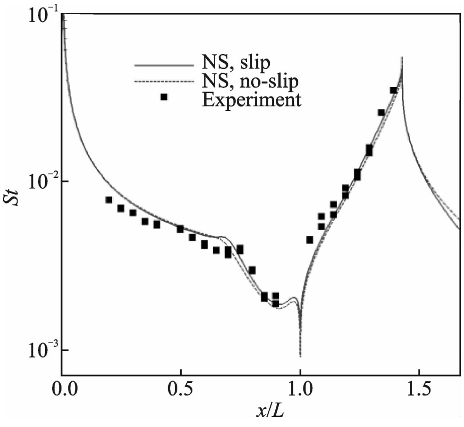

Fig. 11 Stanton number along the surface using different boundary conditions

tions, which is also shown in the Table 1. The "CFD-S" cases are simulated using the slip boundary conditions.

3.2 Sharp double cone

Hypersonic flow of nitrogen around a 25°/55° sharp cone (SDC) is calculated. The configuration and the sample mesh are shown in Fig. 12. The inflow conditions correspond with the RUN 7 experimental conditions in the Calspan-University at Buffalo Research Center (CUBRC) 48-inch shock tunnel.

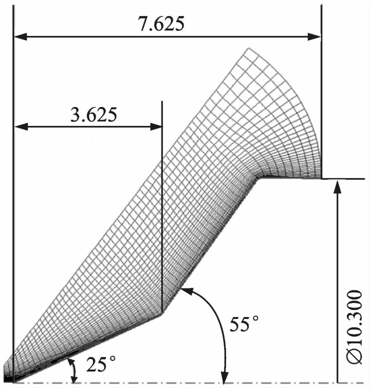

Fig. 12 The configuration and computational mesh for the 25°/55° SDC (unit: inch)

The freestream conditions are: $Ma_\infty = 15.6$, $Re_\infty = 1.375\times10^5/\mathrm{m}$, $T_\infty = 42.6$ K, $T_w = 297$ K. A laminar flow is also ensured in the condition. The Sutherland law is used for modeling the dynamic viscosity, where the related parameters are the same as the HCEF case. The setup of boundary conditions is also the same as those in the HCEF case.

3.2.1 Flow structures

The complex interaction structures are presented in Fig. 13. The oblique shock formed from the first cone combines with the separation shock, forming a merged shock which impinges on the bow shock caused by the second cone. Meanwhile, the supersonic jet is formed behind the shocks. The pressure contours and streamlines at the corner are also shown in Fig. 13. The shock waves and the vortex structures are clearly to be seen. The separation vortex is generated due to the viscous boundary layer and the geometry deflection.

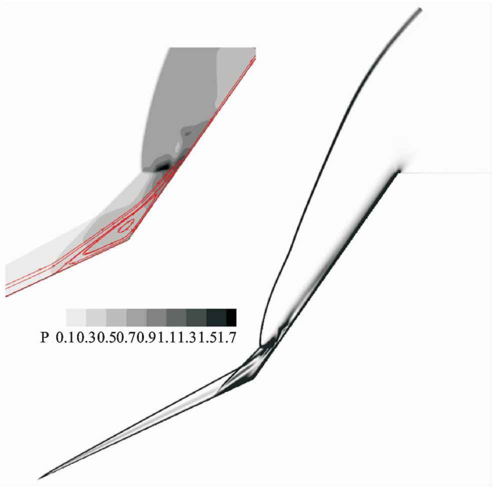

Fig. 13 Numerical schlieren picture, pressure contours and streamlines at the corner

3.2.2 Mesh convergence

Four different meshes are conducted to validate the numerical results of the study. The number of mesh points are 133×64, 266×128, 512×256 and 738×384 in the streamwise and the normal directions, whose corresponding computational cases are denoted as CFD1, CFD2, CFD3 and CFD4, respectively. Table 2 presents the separation and reattachment point locations with different meshes. The recirculation region length increases with the mesh refinement, which is similar to the phenomenon in the HCTF case. Figs. 14, 15 show the pressure and the heat transfer along the surface with the aforementioned four meshes using the no-slip boundary conditions. It can be seen that the physical quantities are mesh convergent.

Table 2 Separation and reattachment point locations for different meshes of SDC

Case	Mesh	Wall BCs	X_s/mm	X_r/mm
CFD1	133×64	No-slip	81.2	99.4
CFD2	266×128	No-slip	79.0	101.0
CFD3	512×256	No-slip	78.1	101.6
CFD4	738×384	No-slip	78.0	101.7
CFD4-S	738×384	Slip	78.1	101.7
DSMC[27]	—	—	80.4	100.8

3.2.3 Computations with slip boundary conditions

To show the local extent of rarefaction, Kn_{GLL} contours is presented in Fig. 16. The con-

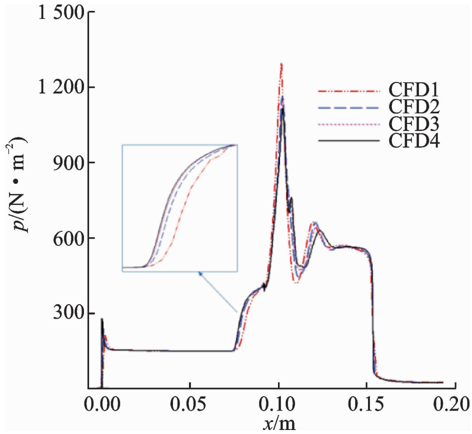

Fig. 14 Pressure along the surface using different meshes

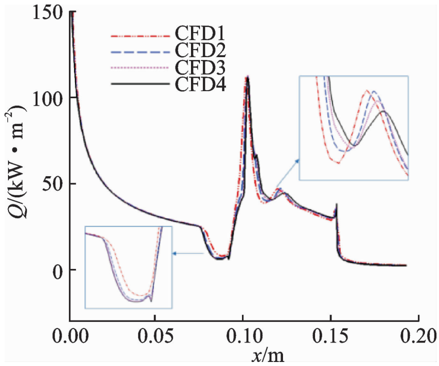

Fig. 15 Heat transfer along the surface using different meshes

tinuum breakdown occurs in the shock region, the thin boundary layer along the surface of first cone, and the second corner. Fig. 17 provides the slip velocity distributions along the surface. By the modification of the formula $u_g = 0.696u_s$, the N-S result agrees well with the DSMC result[27]. As shown in Figs. 18, 19, the pressure and heat transfer distributions along the surface calculated with the fine mesh (738 × 384) are presented. The pressure agrees well with the experimental data[28], and the heat transfer is slightly lower than the experiment. The divergence is about 15% before the separation point and 20% after the reattachment point. Compared with no-slip boundary conditions, the slip ones generate some different results in the leading edge and the first cone where the Kn_{GLL} is greater than 0.05. Regarding the separation zone, the size by slip boundary conditions is slightly smaller than that by the no-slip boundary conditions results. The results indicate that it has few rarefied effects in this case.

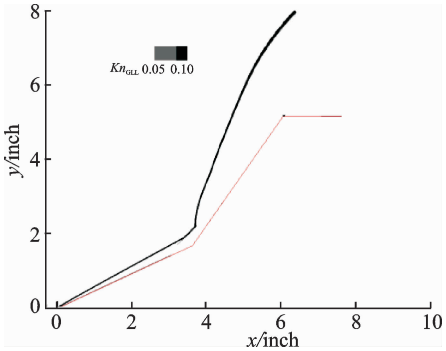

Fig. 16 Kn_{GLL} field for 25°/55° SDC

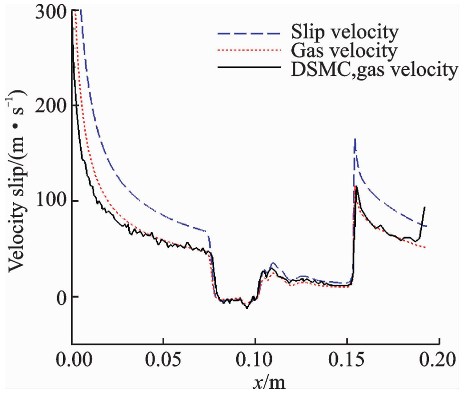

Fig. 17 Slip velocity along the surface for SDC

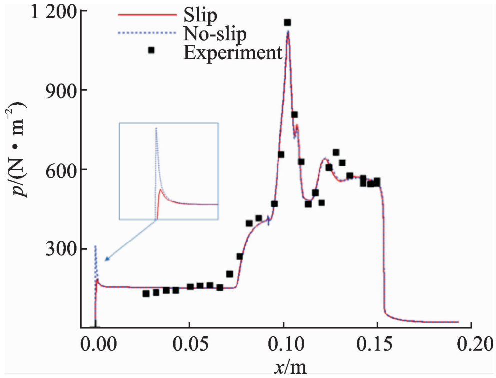

Fig. 18 Pressure along the surface using different boundary conditions

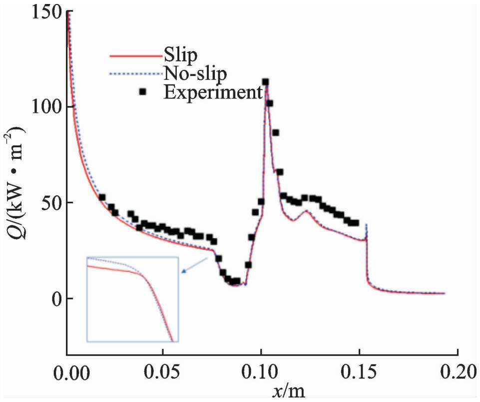

Fig. 19 Heat transfer along the surface using different boundary conditions

4 Conclusions

Hypersonic shock wave/boundary layer interactions with different boundary conditions are simulated and discussed by the WENO-OS3 scheme in this paper.

The main goal of this study is to present a new scheme, i. e. WENO-OS3 scheme, for hypersonic flows. It has the same stencils as NND scheme when constructing fluxes at half nodes, but has higher resolution than NND and WENO3 scheme. Then, the WENO-OS3 scheme is applied to investigate hypersonic flows around the hollow cylinder truncated flare and the 25°/55° sharp double cone with different boundary conditions on several different density meshes. The present studies indicate that (1) the WENO-OS3 scheme has a good capability on predicting heat transfer and a high resolution on capturing the shock waves, expansion waves and other complex fluid structures; (2) good mesh convergent are achieved in both problems, and the recirculation region length increases with the mesh refinement; (3) considering the rarefied gas effect near the surface, the slip boundary conditions are employed, with which the separation region at the corner is smaller and its predictions on pressure and heat transfer are more accurate compared with those results using no-slip boundary conditions. In conclusion, the present study reveals a good performance of the new WENO-OS3 scheme in hypersonic shock wave/boundary layer interactions. It will be used for more complicated simulations and engineering applications in the future.

Acknowledgment

This work was supported by the National Key Basic Research and Development Program (No. 2014CB744100).

References:

[1] HOLDEN M S, WADHAMS T P, MACLEAN M. A review of experimental studies with the double cone and hollow cylinder / flare configurations in the LENS hypervelocity tunnels and comparisons with Navier-Stokes and DSMC computations: AIAA Paper 2010-1281[R]. USA: AIAA, 2010.

[2] LOFTHOUSE A J. Nonequilibrium hypersonic aerothermodynamics using the direct simulation Monte Carlo and Navier-Stokes models [D]. Michigan: the University of Michigan, 2008.

[3] MAXWELL J C. On stresses in rarefied gases arising from inequalities of temperature[J]. Philosophical Transactions of the Royal Society, 1879, 170: 231-256.

[4] VON SMOLUCHOWSKI M. Über wärmeleitung in verdünnten gasen [J]. Annalen der Physik und Chemie, 1898, 64: 101-130. (in German)

[5] GÖKÇEN T, MACCORMACK R W, CHAPMAN D R. Computational fluid dynamics near the continuum limit: AIAA Paper 87-1115 [R]. USA: AIAA, 1987.

[6] GÖKÇEN T, MACCORMACK R W. Nonequilibrium effects for hypersonic transitional flows using continuum approach: AIAA Paper 1989-0461[R]. USA: AIAA, 1989.

[7] LOCKERBY D A, REESE J M, GALLIS M A. Capturing the Knudsen layer in continuum-fluid models of nonequilibrium gas flows [J]. AIAA Journal, 2005, 43(6): 1391-1393.

[8] DEISSLER R. An analysis of second-order slip flow and temperature-jump boundary conditions for rarefied gases [J]. International Journal of Heat and Mass Transfer, 1965, 7: 681-694.

[9] YILDIZ B, GOKTURK T. An extension to the first order slip boundary conditions to be used in early transition regime: AIAA Paper 2002-2779 [R]. USA: AIAA, 2002.

[10] NAM T P, LE C W, JASON M R, et al. Langmuir-Maxwell and Langmuir-Smoluchowski boundary conditions for thermal gas flow simulations in hypersonic aerodynamics [J]. International Journal of Heat and Mass Transfer, 2012, 55: 5032-5043.

[11] ZHANG H X, ZHUANG F G. NND schemes and their applications to numerical simulation of two- and three- dimensional flows [J]. Advances in Applied Mechanic, 1991, 29: 193-256.

[12] LIU X, OSHER S, CHAN T. Weighted essentially non-oscillatory schemes [J]. Journal of Computational Physics, 1994, 115: 200-212.

[13] JIANG G S, SHU C W. Efficient implementation of weighted ENO schemes [J]. Journal of Computational Physics, 1996, 126(1): 202-228.

[14] SHEN Y Q, ZHA G C, HUERTA M A. Simulation of hypersonic shock wave/boundary layer interaction using high order WENO scheme: AIAA Paper 2010-1047[R]. USA: AIAA, 2010.

[15] LIU X, DENG X G. Application of high-order accurate algorithm to hypersonic viscous flows for calculating heat transfer distributions: AIAA Paper 2007-691 [R]. USA: AIAA, 2007.

[16] OLIVEIRA M L, XIE P, SU J Z, et al. Modified weighted compact scheme for shock-boundary layer interaction and double cone: AIAA Paper 2008-755 [R]. USA: AIAA, 2008.

[17] LI Chen. Investigations on some issues in accurate aerodynamic and aerothermal computation in hypersonic flows [D]. Mianyang: China Aerodynamics Research and Development Center, 2014. (in Chinese)

[18] LI Q, GUO Q L, SUN D, et al. A fourth-order symmetric WENO scheme with improved performance by new linear and nonlinear optimizations [J]. J Sci Comput, 2017, 17:109-143.

[19] SHU C W, OSHER S. Efficient implementation of essentially non-oscillatory shock-capturing schemes [J]. Journal of Computational Physics, 1989, 83: 32-78.

[20] MACCORMACK R W. A numerical method for solving the equations of compressible viscous flow [J]. AIAA Journal, 1982, 20(9): 1275-1281.

[21] BECKER M. Flat plate flow field and surface measurements from merged layer into transition regime [C]// Proceedings of the seventh International Symposium on Rarefied Gas Dynamics. [S. l.]:[s. n.],1969: 515-528.

[22] BOYD I D, CHEN G, CANDLER G V. Predicting failure of the continuum fluid equations in transitional hypersonic flows [J]. Physics of Fluids, 1995, 7 (1): 210-219.

[23] GORCHAKOVA N, KUZNETSOV L, YARYGIN V. Progress in hypersonic studies using electron-beam-excited X-Ray detection [J]. AIAA Journal, 2002, 40(4): 593-598.

[24] MARKELOV G N, KUDRYAVTSEV A N, IVANOV M S. Continuum and kinetic simulation of shock wave/laminar boundary layer interaction in hypersonic flows: AIAA Paper 1999-3527[R]. USA: AIAA, 1999.

[25] LI Q B, FU S. Application of gas-kinetic scheme with kinetic boundary conditions in hypersonic flow [J]. AIAA Journal, 2005, 43(10): 2170-2176.

[26] MORTAZAVI M, KNIGHT D. Shock wave boundary layer interaction in a hypersonic laminar flow on a hollow cylinder flare: AIAA Paper 2016-0351 [R]. USA: AIAA, 2016.

[27] JAMES N M, BIRD G A. Direct simulation Monte Carlo simulations of hypersonic flows with shock interactions [J]. AIAA Journal, 2005, 43(12): 2565-2573.

[28] HOLDEN M S, WADHAMS T P, CANDLER G V, et al. Measurements in regions of low density laminar shock wave/boundary layer interaction in hypervelocity flows and comparison with Navier-Stokes predictions: AIAA Paper 2003-1131[R]. USA: AIAA, 2003.

Mr. **Li Chen** received his B. S. degree in School of Aerospace Engineering from Beijing Institute of Technology, Beijing, China, in 2011 and M. E. degree in Fluid Mechanics from China Aerodynamics Research and Development Center (CARDC), Mianyang, China, in 2014. In July 2011, he joined the State Key Laboratory of Aerodynamics (SKLA), Mianyang, China.

Mr. **Guo Qilong** received his B. S. degree in Thermal Science and Energy Engineering from University of Science and Technology of China, Hefei, China, in 2010 and M. E. degree in Fluid Mechanics from CARDC, Mianyang, China, in 2013. In July 2010, he joined the SKLA, Mianyang, China.

Prof. **Li Qin** received his B. S. degree in School of Aerospace Engineering from National University of Defense Technology, Changsha, China, in 1991. He currently works in the SKLA, Mianyang, China.

Prof. **Zhang Hanxin** is an academician of Chinese Science Academy. He currently works in National CFD Laboratory of Aerodynamics, Beihang University, Beijing, China.

(Executive Editor: Xu Chengting)